Extrinsic and Depth Calibration of ToF-cameras

Stefan Fuchs and Gerd Hirzinger
DLR, Institute of Robotics and Mechatronics
Oberpfaffenhofen, Germany
{stefan.fuchs, gerd.hirzinger}@dlr.de

Abstract

Recently, ToF-cameras have attracted attention because of their ability to generate a full $2\frac{1}{2}$D depth image at video frame rates. Thus, ToF-cameras are suitable for real-time 3D tasks such as tracking, visual servoing or object pose estimation. The usability of such systems mainly depends on an accurate camera calibration. In this work a calibration process for ToF-cameras with respect to the intrinsic parameters, the depth measurement distortion and the pose of the camera relative to a robot's endeffector is described. The calibration process is not only based on the monochromatic images of the camera but also uses its depth values that are generated from a chequer-board pattern. The robustness and precision of the presented method is assessed applying it to randomly selected shots and comparing the calibrated measurements to a ground truth obtained from a laser scanner.

1. Introduction

A wide range of digital image processing methods such as image segmentation, image understanding, or pattern recognition are used for contactless surveillance of the environment, to track objects or detect obstacles. However, numerous applications *e.g.* driver assistance systems or robotic tasks have to infer 3D information from the 2D image processing results, since the distance of perceived obstacles or the pose of tracked objects is required. Generally, common stereo vision methods or structure-from-motion (SFM) algorithms are used but endued with disadvantages. As correspondences in at least two images must be sought, stereo and SFM-algorithms are computationally very complex and therefore, critical. Moreover, the necessary search for correspondences is prone to errors due to possible misassignments in homogenous textures.

The ToF-camera technology outweighs these disadvantages. ToF-cameras provide a monochromatic image allowing for classical image processing algorithms and additionally measure distances for all pixels. Thereto, the observed scene is illuminated with modulated infrared light. The reflected light features a phase-delay that is detected within the pixels and directly translated into a distance value. Thus, the ToF-camera provides $2\frac{1}{2}$D depth information of dynamic or static scenes at video frame rates, irrespective of the object's texture. Due to these properties the camera is suited for a wide range of applications, such as tracking, object detection, pose estimation and collision avoidance.

At the time, depth measurements with ToF-cameras are still very erroneous. Accounting the complex electronic measuring principle, the measured distances depend on the exposure time and the reflectivity of the observed objects. The understanding of these errors and the development of appropriate error models are crucial for upgrading the ToF-camera from a sensor to a measurement device. The manufacturers of ToF-cameras handle these problems with different calibration procedures. However, the used calibration methods are costly because the entire working range is taken into account although many users only run the camera within a limited working range. Current ToF-camera calibration approaches perform a linear mapping, assuming the error to be a fixed pattern noise or adjust range measurement errors by using look-up-tables or splines.

In contradiction, this work presents a calibration procedure that enables the user to calibrate the distance-related and the amplitude-related error of a ToF-camera for a desired operating range and in addition determines the extrinsic parameters of the ToF-camera. The outline of this paper is organised as follows: Section 2 discusses related work with TOF-camera calibration methods. Section 3 develops the error model, which is used in section 3.3 to derive an optimal calibration method. Experiments and results of the calibration approach are presented in section 4 and finally concluded in section 5.

2. Related Work

Hereafter, the calibration procedure of a ToF-camera is considered for three distinct sets of parameters. Since the ToF-camera features a pinhole-camera model, its parameters - optical center, focal length and lens distortion - are

978-1-4244-2243-2/08/$25.00 ©2008 IEEE

determined by an intrinsic calibration. Additionally to standard intrinsic parameters a depth calibration determines the distance measurement errors of the ToF-camera. Lastly, the camera's extrinsic parameters w.r.t. an external positioning system *e.g*. a robot or an optical tracking system are determined. The common procedure according to Zhang [10] is suggested for the intrinsic calibration of the ToF-camera. The relationship between measurement points in the image and their known positions is used to determine the intrinsic parameters by utilising common tools *e.g*. Calde/Callab, Matlab-Toolbox, or OpenCV. While Kahlmann *et al*. propose in [4] and [5] a calibration pattern consisting of filled white circles on a black background, Fuchs *et al*. in [2] use a classic chequer-board pattern. Both procedures are suited to accurately determine the intrinsic parameters.

By contrast, Beder *et al*. in [1] develops a different approach. In addition to the monochromatic images of the chequer-board Beder *et al*. incorporates the measured depth values. Thus, the intrinsic parameters and the pose of the camera w.r.t. the calibration pattern are determined requiring only a single image. But, since the lens distortion and distance measurement errors are neglected, this method yields a lack of precision.

In [5] and [4] Kahlmann *et al*. identify the distance-related error at various exposure times and store it for later corrections in a look-up-table. In [6] Lindner uses B-splines to describe the distance-related error. Both, Kahlmann and Lindner determine the distance-related error using a high precision optical measurement rack.

Furthermore, in [7] Lindner estimates the amplitude-related error in addition to the distance-related error. Lindner presents a procedure that uses a second monochromatic camera instead of a measurement rack. This camera captures images of a chequer-board pattern whose pose w.r.t. the monochromatic camera is estimated. The monochromatic camera's pose w.r.t. the ToF-camera is known, too. Thus, in a first step the distance-related error is estimated. In a second step, the amplitude-related error is determined on a grey-scaled pattern. As a result this procedures yields an overall precision of $10\mathrm{mm}$. Actually, for a closer measurement range (less than $1300\mathrm{mm}$) $4\mathrm{mm}$ are indicated.

This paper presents an improved depth calibration procedure for a ToF-camera featuring two advantages over the formerly named procedures: Firstly, the calibration simply bases on the measured values of the ToF-camera (in terms of amplitude and depth) and on an external positioning system, *e.g*. a robot or optical tracking system. No additional camera is necessary, the pose of the calibration plane and of the ToF-camera w.r.t. the positioning system (also referred to as sensor-to-TCP[1]-transformation) are determined concurrently. Secondly, all parameters of the ToF-camera error model are estimated simultaneously.

[1]Tool-center-point

3. Distance-Error-Model

Within the the following sections the error model for the depth calibration is described. The error model incorporates three errors: a distance-related error, an amplitude-related error and a latency-related error. First of all, a short introduction into the ToF-camera measurement principle is given. The ToF-camera uses the principle of modulation interferometry. An illumination module attached to the camera emits incoherent near-infrared (NIR) light $g(t)$

$$g(t) = \cos(\omega t) \tag{1}$$

that is sinusoidal modulated with a frequency ω. This light illuminates the focused 3D scene. The diffusely remitted light $s(t)$

$$s(t) = k + a\cos(\omega t + \phi) \tag{2}$$

transports the distance information in terms of a phase-delay ϕ w.r.t. the emitted signal $g(t)$. Further, the emitted signal is tagged with the amplitude of remission a and an unmodulated constant component k resulting from the background illumination. The phase-delay ϕ between the signals $g(t)$ and $s(t)$ can be estimated by the so-called 4-phase-algorithm. Thereto, the correlation $c(\tau)$

$$c(\tau) = (s * g)(\tau) = h + \frac{a}{2}\cos(\omega\tau + \phi) \tag{3}$$

between the emitted and remitted signal is computed for 4 internal phase-delays $\tau_p = p\frac{\pi}{2}, p = 0, 1, 2, 3$. Given the speed of light c and the frequency of modulation ω, 4 correlations $R_p = c(\tau_p)$ are generated in order to compute the phase-delay ϕ

$$\phi = \arctan(\frac{R_1 - R_3}{R_0 - R_2}) \quad , \tag{4}$$

the amplitude a

$$a = \frac{\sqrt{(R_1 - R_3)^2 + (R_0 - R_2)^2}}{2} \quad , \tag{5}$$

and the distance d

$$d = \frac{c\phi}{4\pi\omega} \tag{6}$$

for a single pixel.

Let $\mathbf{P} = \{\mathbf{v}_1, ..., \mathbf{v}_W\}$ represent W image coordinates with $\mathbf{v} = (r, c)$, where r and c denote the image row and column. The pairs of N amplitude images and depth images (with distorted depth measurements) are denoted by $(A^i(\mathbf{v})|i = 1, ..., N)$ and $(D^i(\mathbf{v})|i = 1, ..., N)$ respectively.

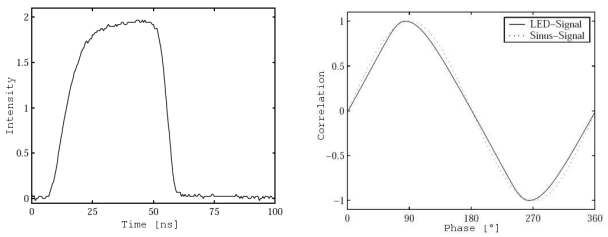

Figure 1. The left diagram shows the asymmetric response of an NIR-LED-signal with different rise and fall times. The impact of the non-ideal respose of the NIR-LEDs on the correlation of the LED-signals with the control signal is plotted in the right diagram. [8]

3.1. Distance-and Amplitude-Related Errors

In the following section the impact of the non-ideal response of the NIR-LEDs and the strength of the the remitted signal on the distance measurement is discussed.

Figure 1 pictures the optical response of a NIR-LED with its characteristic rising and falling edges. An asymmetric signal with different rise and fall times is recognisable. It is obvious that the correlation of this LED-signals with the control signal $g(t)$ results in a non-harmonic sinusoidal curve w.r.t. $g(t)$ (see Figure 1). Since a harmonic curve is a basic assumption for the 4-phase-algorithm, applying this algorithm on non-ideal signals results in a phase-delay-related and distance-related error respectively.

This systematic distance-related error increases with the discrepancy between the ideal and non-ideal signals. However, the distance-related error can be corrected, if the response of the NIR-LEDs is known. Given that the NIR-LED signal is reproducible, the distance-related error is deterministic and can be compensated by a look-up-table. However, the ToF-camera illumination features several NIR-LEDs whose responses are hardly to identify. Thus, the error can be derived from the distance measurements and compensated.

The remitted signal $s(t)$ and emitted signal $g(t)$ are directly correlated in the solid-state CMOS sensor pixels. The emitted signal serves the sensor pixel as a reference signal $s_\tau(t)$ for the demodulation annotated with a relative phase-delay τ_i. The incident photons activate the semi-conductor to generate electrons that are forced by $s_\tau(t)$ to accumulate in two integrational capacitors where they are stored and read out by a controller. The difference between these two integrational capacitors corresponds to the correlation $c(\tau_i)$ and is proportional to the phase-delay ϕ. Due to non-linearities of the semiconductor and in account of imperfect separation properties a different number of incident photons at a constant distance causes different distance measurements. Furthermore, this amplitude-related error changes also with the distance. Within this work the distance- and amplitude-related errors are joined and approximated by M penalised splines $(E_{\mathrm{d}}^m(D^i(\mathbf{v}))|m = 1...M$. The number M depends on the amplitude grouping. Thereby, every single spline represents the distance-related error for an amplitude interval $[I_{start}^m, I_{end}^m]$. A single spline $E_{\mathrm{d}}^m(D^i(\mathbf{v}))$ with maximum order p

$$E_d^m(D^i(\mathbf{v})) = \delta_0^m + \delta_1^m D^i(\mathbf{v}) + ... + \delta_p^m D^i(\mathbf{v})^p + \sum_{k=1}^{K} \delta_{p+k}(D^i(\mathbf{v}) - \kappa_k)_+^p \quad (7)$$

is characterised by the spline coefficients $[\delta_0^m, ..., \delta_p^m, \delta_{p+1}^m, ..., \delta_{p+k}^m]$ and the K knot points $\{\kappa_k^m\}_{k=1}^K$.

3.2. Latency-Related Error

The phase-delay originates partially from latencies on the sensor due to signal-propagation-delays and semiconductor properties. Since the emitted and remitted signals are correlated directly on the sensor array, different latencies for every pixel have to be taken into account. Thus, a latency-related error $E_{\mathrm{l}}(\mathbf{v})$

$$E_{\mathrm{l}}(\mathbf{v}) = b_0 r + b_1 c \quad (8)$$

is approximated by the parameters b_0 and b_1.

3.3. Depth Calibration

The overall error $C(D^i(\mathbf{v}), A^i(\mathbf{v}), \mathbf{v})$ is defined by

$$C(D^i(\mathbf{v}), A^i(\mathbf{v}), \mathbf{v}) = E_{\mathrm{d}}(.) + E_{\mathrm{l}}(.) \quad (9)$$

and the corrected distance $\hat{D}^i(\mathbf{v})$ is denoted by

$$\hat{D}^i(\mathbf{v}) = D^i(\mathbf{v}) - C(D^i(\mathbf{v}), A^i(\mathbf{v}), \mathbf{v}) \quad . \quad (10)$$

Within a calibration step, the set $\mathbf{S}$ of error model parameters has to be estimated. $\mathbf{S}$ includes the spline coefficients $\{\delta_0^m, ..., \delta_p^m, \delta_{p+1}^m, ..., \delta_{p+k}^m\}_{m=1}^M$ and (b_1, b_2). For the proposed calibration procedure, a robot serves as external positioning system. The ToF-camera is mounted on the robot and moved to $i = 1, ..., N$ different poses ${}^{\mathrm{w}}\mathbf{T}_{\mathrm{t}}^i$. A chequerboard pattern is used as calibration plane in order to capture dark and bright areas. The calibration plane is defined by its normal $\mathbf{n}_c$ and its distance d_c to the origin of world coordinate system. The poses ${}^{\mathrm{w}}\mathbf{T}_{\mathrm{t}}^i$ are given by the robot control. In Figure 2 the setting is sketched. Let Ω transform a distance value $\hat{D}^i(\mathbf{v})$ from the polar sensor coordinate system to the Cartesian sensor coordinate system and $\Pi(\Omega(\hat{D}^i(\mathbf{v})))$ project a Cartesian depth value $\Omega(\hat{D}^i(\mathbf{v}))$ with

$$\Pi(M(\hat{D}^i(\mathbf{v}))) = \Omega(\hat{D}^i(\mathbf{v})) \begin{bmatrix} \frac{(c-u_0)}{\alpha} \\ \frac{(r-v_0)}{\beta} \\ 1 \end{bmatrix} \quad (11)$$

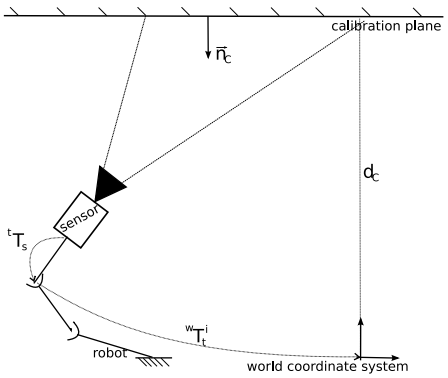

Figure 2. Sketch of the experimental setup for depth calibration and hand-eye-calibration. The calibration plane is measured from different poses ${}^{w}\mathbf{T}_t^i$. A nonlinear optimisation algorithm is used in order to estimate the parameter set $\mathbf{S}$ including the sensor-to-TCP transformation ${}^{t}\mathbf{T}_s$, the depth correction parameters and the pose of the calibration plane $(\mathbf{n}_c, d_c)$ with respect to the world coordinate system.

into a Cartesian sensor coordinate system. The distance $f_{\mathbf{v}}^i$ between an measured point $\mathbf{v}$ and the calibration plane in a single shot i

$$f_{\mathbf{v}}^i = \mathbf{n}_c^T [\,{}^{\mathrm{w}}\mathbf{T}_{\mathrm{t}}^i\,{}^{\mathrm{t}}\mathbf{T}_{\mathrm{s}}\,\Pi(\hat{D}^i(\mathbf{v}))] - d_c \tag{12}$$

can be estimated with a robot pose ${}^{\mathrm{w}}\mathbf{T}_{\mathrm{t}}^i$ and a known sensor-to-TCP transformation ${}^{\mathrm{t}}\mathbf{T}_{\mathrm{s}}$ as well as a known pose of the calibration plane $(\mathbf{n}_c, d_c)$. The hand-eye-transformation ${}^{\mathrm{t}}\mathbf{T}_{\mathrm{s}}$ and the pose of the calibration wall $(\mathbf{n}_c, d_c)$ are unknown as well as the distance $D^i(\mathbf{v}))$ is erroneous $f_{\mathbf{v}}^i$ is not assumed to be zero. Therefore, $\mathbf{S}$ is extended by $(\mathbf{n}_c, d_c)$ and ${}^{\mathrm{t}}\mathbf{T}_{\mathrm{s}}$ so that $\mathbf{S}$ can be estimated by minimising the error function

$$F(\mathbf{S}) = \frac{1}{2}\sum_{i=1}^{N}\sum_{\mathbf{v}\in\mathbf{P}} f_{\mathbf{v}}^i(.)^2 \tag{13}$$

over all shots.

4. Experiments and Results

Experiments are performed with the IFM O3D100 (www.ifm.de) ToF-camera. The O3D100 camera is characterised by a very compact design and protected against splash water or dust. Thus, the camera is appropriate for industrial applications. The O3D100 camera has a resolution of 50×64 pixels and covers a measurement range up to $7500\ \mathrm{mm}$. Furthermore, it features suppression of background illumination. The standard deviation varies between $2\ \mathrm{mm}$ and $8\ \mathrm{mm}$ depending on the measured distance. The intrinsic parameters of the ToF-camera are estimated using the common tool CalDe/Callab [3].

The IFM O3D100 is added to the experimental setup of the DLR 3D-Modeler [9] which is attached to the TCP of

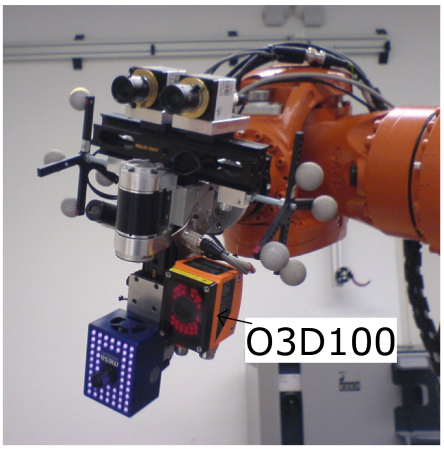

Figure 3. Experimental setup of DLR 3D-Modeler with the IFM O3D100 ToF-camera

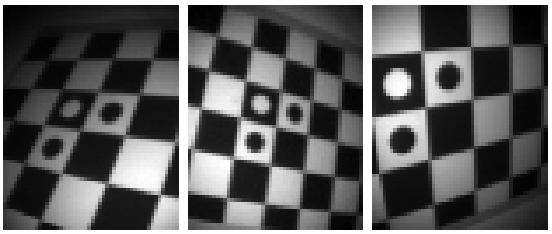

Figure 4. Of the overall image set, which is used for the intrinsic, extrinsic and depth calibration steps, three exemplary images are shown.

a standard industrial robot, type KUKA KR 16 (see Figure 3 for an image of the sensor configuration). The robot is moved to different positions in order to capture the required images. The TCP pose for every image is given by the robot control with a precision of $1\ \mathrm{mm}$ in translation and $0.1°$ in rotation.

The calibration approach is evaluated by the means of robustness, precision and validity. 50 shots are captured at 3 different exposure times ($1000\ \mu s$, $1500\ \mu s$, $2000\ \mu s$, see Figure 4) with different angles and distances to the plane. $\mathbf{S}$ consists of 149 parameters. Besides the extrinsic parameters, 8 splines are estimated for depth correction. The distances vary between $500\ \mathrm{mm}$ and $1500\ \mathrm{mm}$. The real pose of the calibration plane is determined with a laser range scanner. The laser range scanner is more precise as a ToF-camera and therefore, assumed to provide the ground truth: $(\mathbf{n}_c = [0.9982, -0.0588, 0.0023], d_c = 1969.01\mathrm{mm})$. Since the ground truth is also estimated by the calibration step, it is only measured for verification purposes.

	1000μs		1500μs		2000μs	
	μ	σ	μ	σ	μ	σ
d_c/mm	1969.5	2.6	1968.0	3.1	1973.0	4.2
t_x/mm	130.4	5.6	131.3	5.1	130.4	6.0
t_y/mm	46.4	3.7	46.1	2.7	43.8	4.1
t_z/mm	-46.3	5.2	-43.6	4.1	-46.2	5.1

Table 1. Evaluation of robustness. As a result of the applied calibration algorithm on 1000 samples each with 18 randomly selected shots the mean value μ and standard deviation σ of the calib plane distance d_c and the translational components of the extrinsic parameters t_x,t_y,t_z are presented within the table.

	$1000\mu s$		$1500\mu s$		$2000\mu s$	
	μ	σ	μ	σ	μ	σ
	$/mm$	$/mm$	$/mm$	$/mm$	$/mm$	$/mm$
Stage 1	-12.7	15.3	-14.6	18.9	-44.7	28.5
Stage 2	-1.1	4.5	-1.2	4.8	-0.1	5.7

Table 2. The estimated set **S** of depth correction parameters is progressively applied to the measured depth values in order to demonstrate the increasing precision. The distance error is computed by substracting the corrected depth values from the ground truth that is estimated with a laser range scanner. At *Stage 1* just a global distance offset is considered. At *Stage 2* the complete error model is applied.

4.1. Robustness

The analysis of robustness focuses on two questions: Does the error model assumptions cover the real sensor behaviour and is the calibration procedure robust w.r.t. the chosen shot samples? These issues are investigated by randomly taking a number of shots and applying the proposed calibration procedure to each. The results are presented in Table 1. The average poses of the calibration plane and the sensor's pose w.r.t. the TCP are determined with an standard deviation of $5\ \mathrm{mm}$ (see Figure 1). The results of d_c meet the measured ground truth and are nearly equal for all integration times.

The outcomes of this investigation indicate, that the presented error model covers the real sensor behavior and that the calibration process is robust w.r.t. the chosen shot samples and different integration times.

4.2. Precision

Secondly, the precision is investigated. Initially, the calibration procedure is applied to a representative sample of shots. Figure 5 plots the resulting correction splines. This calibration result is analysed by two methods. At first, the calibrated depth measurements are projected into the world coordinate system. If these measurements were error free and the sensor-to-TCP transformation was correct,

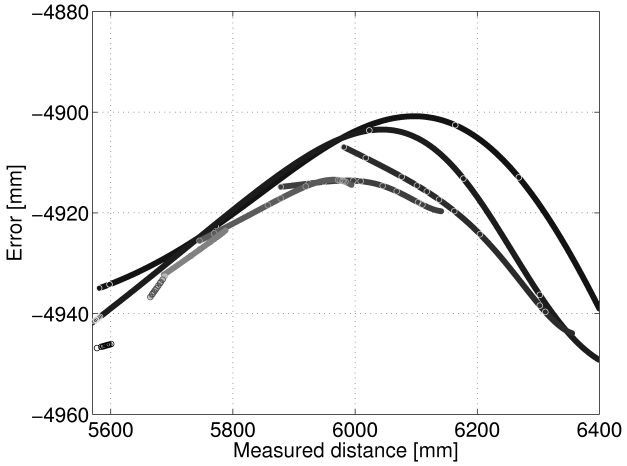

Figure 5. The resulting splines of a depth calibration are plotted. Every spline represents the depth correction for a special amplitude and distance interval. The curves indicate, that the distance correction increases with the amplitude interval, that is covered by a spline. (the higher the amplitude, the brighter the spline) Furthermore, an overall sinusoidal curve of the distance-related error is apparent.

	1000μs		1500μs		2000μs	
	$\mu/^\circ$	$\sigma/^\circ$	$\mu/^\circ$	$\sigma/^\circ$	$\mu/^\circ$	$\sigma/^\circ$
Stage 1	3.6	2.2	3.4	2.1	5.0	2.3
Stage 2	1.6	1.0	1.6	1.4	2.6	1.73

Table 3. The estimated set **S** of depth correction parameters is applied to the measured depth values demonstrating the increasing precision. The covariance of a measured point cloud is computed in order to estimate the pose of this plane. The table lists the average angle with that all planes subtend each other. At *Stage 1* just a global distance offset is considered. At *Stage 2* all errors are corrected.

the measured planes would fit perfectly. Hence, the distances and angles between these planes would be zero. This method is suited to evaluate the angle precision of the estimated sensor-to-TCP transformation. At second, the calibrated depth measurements of the calibration plane are projected into the world coordinate system and compared to the ground truth measured by the laser scanning system.

As shown in Table 2 and 3 the precision increases applying the depth calibration. An average precision of 2° and $1\ \mathrm{mm}$ with a standard deviation of $5\ \mathrm{mm}$ is reached. The investigations verify the calibration results to be very precise. In Figure 6 the uncalibrated and calibrated measurement data is plotted exemplarily.

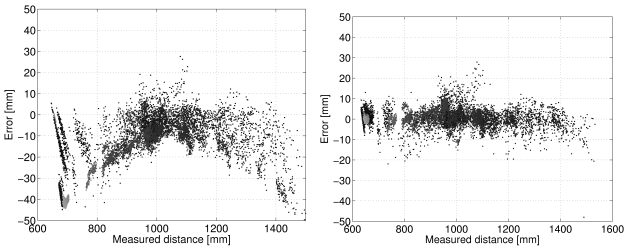

Figure 6. Both diagrams plot the distance measurement error for each single pixel referred to the ground truth measured with a laser scanner. The pixels are grey-scaled with their amplitude values (the lower, the darker). The uncalibrated measurements in the left diagram enclose the distance and amplitude related error that is corrected within the right diagram.

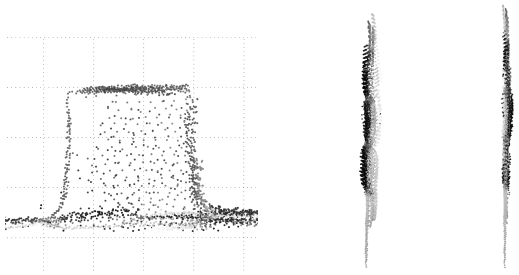

Figure 7. Validity of calibration. The left image depicts the reconstructed cube and the matching cube faces. The gridsize is $50\ \mathrm{mm}$. The two right graphs point out the improvement of correcting the amplitude related error. While the left plane is rough because of the different distance measurements for dark and bright areas, the right plane is smoother.

4.3. Validity

In the following, the validity for a different working range is analysed. Therefore, a cube standing on a chequerboard is circumferentially $(270°)$ observed from a number of different poses. The result is plotted in Figure 7. The figure shows a good alignment of all measurements. The size of the cube nearly meets the real size of $140\ \mathrm{mm}$. Furthermore, the correction of the amplitude-related error is illustrated in Figure 7.

5. Conclusion

Within this work a novel calibration procedure is presented. The calibration procedure simultaneously estimates the distance parameters and the the extrinsic parameters for a ToF-camera, requiring only the distance and amplitude measurements w.r.t. an external positioning system. Neither a ground truth *e.g*. from a high end measurement rack nor an additional monochromatic camera are needed. The calibration procedure considers the distance-related, the amplitude-related and the latency-related error simultaneously. Thus, the calibration procedure is simplified. As a result, the robustness and the achievable precision of this calibration method are demonstrated exemplarily with an O3D100 ToF-camera. An overall mean precision of $1\ \mathrm{mm}$ and $2°$ is achievable and recommends the ToF-cameras for precise robotic applications *e.g*. visual servoing or grasping tasks.

Acknowledgment

This work has been partially funded by the Federal Ministry of Education and Research as part of the integrated project Lynkeus (www.lynkeus-3d.de).

References

[1] C. Beder and R. Koch. Calibration of focal length and 3d pose based on the reflectance and depth image of a planar object. In *Proceedings of the DAGM Dyn3D Workshop, Heidelberg, Germany*, volume I, September 2007.

[2] S. Fuchs and S. May. Calibration and registration for precise surface reconstruction. In *Proceedings of the DAGM Dyn3D Workshop, Heidelberg, Germany*, volume I, September 2007.

[3] Inst. of Robotics and Mechatronics, Available at http://www.robotic.dlr.de/callab/. *Callab 2005 and CalDe*, 2005.

[4] T. Kahlmann and H. Ingensand. Increased accuracy of 3d range imaging camera by means of calibration. In *Optical 3-D Measurement Techniques, Zurich, Switzerland*, July 2007.

[5] T. Kahlmann, F. Remondino, and H. Ingensand. Calibration for increased accuracy of the range imaging camera swissranger. In *Proceedings of the ISPRS, Dresden, Germany*, September 2006.

[6] M. Lindner and A. Kolb. Lateral and depth calibration of pmd-distance sensors. In G. Bebis, R. Boyle, B. Parvin, D. Koracin, P. Remagnino, A. V. Nefian, M. Gopi, V. Pascucci, J. Zara, J. Molineros, H. Theisel, and T. Malzbender, editors, *In Procedings of the ISVC, Lake Tahoe, USA*, volume 4292 of *Lecture Notes in Computer Science*, pages 524–533. Springer, 2006.

[7] M. Lindner and A. Kolb. Calibration of the intensity-related distance error of the PMD TOF-Camera. In *SPIE: Intelligent Robots and Computer Vision XXV*, volume 6764, pages 6764–35, 2007.

[8] B. Schneider. *Der Photomischdetektor zur schnellen 3D Vermessung für Sicherheitssysteme und zur schnellen Informationsübertragung im Automobil, Siegen, Germany*. PhD thesis, 2003.

[9] M. Suppa, S. Kielhoefer, J. Langwald, F. Hacker, K. Strobl, and G. Hirzinger. The 3d-modeller: A multi-purpose vision platfrom. In *Proceedings ICRA: International Conference on Robotics and Automation, Rome, Italy*, April 2007.

[10] Z. Zhang. A flexible new technique for camera calibration. *IEEE Transactions on Pattern Analysis and Machine Intelligence*, 22(11):1330–1334, 2000.